Frequency- and time-resolved photocurrents in vacuum-deposited stabilised a-Se films: the role of valence alternation defects

Janet Jacobs[1] · George Belev[2] · Adam Brookfield[1,3] · Floriana Tuna[1,3] · Safa Kasap[4] · Richard J. Curry[1]

Abstract

Stabilised amorphous selenium (a-Se) is currently used in the majority of direct conversion mammographic X-ray imaging detectors due to its X-ray photoconductivity and its ability to be uniformly deposited over large area TFT substrates by conventional vacuum deposition. We report experimental results on photocurrent spectroscopy (frequency-resolved spectroscopy (FRS) and single-time transients), on vacuum-deposited a-Se films. We show that all measured photocurrents depend critically on the relative time spent by the material in the light and in the dark. We identify that the observed pronounced variation in optical response depends on the density of trapped (optically injected) charge within 200 nm of the surface and show that it is the ratio of dark and light exposure time that controls the density of such charge. Our data confirm that the localised charge radically influences the photocurrent transient shape due to the effective screening of the applied field within 200 nm of the surface. The field modification occurs over the optical extinction depth and changes both the photogeneration process and the drift of carriers. Many aspects of our data carry the signature of known properties of valence alternation pair (VAP) defects, which control many properties of a-Se. Modelling in the time domain shows that light generation of VAPs followed by optically triggered VAP defect conversion can lead to near-surface charge imbalance, demonstrating that VAP defects can account for the unusual optical response. The stabilised a-Se films were deposited above the glass transition temperature of the alloy with composition a-Se:0.3% As doped with ppm Cl. Electron paramagnetic resonance measurements at temperatures down to 5 K did not detect any spin active defects, even under photoexcitation above band gap.

1 Introduction

Amorphous chalcogenide semiconductors are used in a variety of electronic and optoelectronic technologies, from phase change memories to multibillion dollar X-ray image detector applications, and especially in mammography [1–5]. Of particular interest among this class of materials is stabilised amorphous selenium (a-Se): a-Se

✉ Janet Jacobs
  janet.jacobs@manchester.ac.uk

✉ Richard J. Curry
  richard.curry@manchester.ac.uk

1 Department of Electronic and Electrical Engineering, Photon Science Institute, University of Manchester, Manchester, UK

2 Saskatchewan Structural Sciences Center, University of Saskatchewan, Saskatoon, Canada

3 Department of Chemistry, University of Manchester, Manchester, UK

4 Department of Electrical and Computer Engineering, University of Saskatchewan, Saskatoon, Canada

that has been alloyed with small amounts of As (less than 1%, typically 0.2–0.5%) to stabilise the structure against crystallisation and doped with a small amount of halogen (Cl) in the ppm range to enhance hole transport [3, 6–8]. a-Se is currently the most successful X-ray photoconductor used in commercial flat panel mammographic X-ray image detectors [9]. It belongs to a special class of non-crystalline solids called amorphous chalcogenide semiconductors [1–3]. While other chalcogenide compositions such as Ag-doped Ge-Te in this group have shown potential for radiation detection [1–12], a-Se is the only commercialised X-ray photoconductor. Current interest lies not only in the use of a-Se but also in polycrystalline Se both for existing technologies and for novel devices which may underpin next generation systems [13–19]. The properties of a-Se have been widely reviewed in the literature and most recently by Tanaka [20]. Extending the functionality of these materials will depend heavily on how such material properties can be controlled in device structures. We note that commercial a-Se detectors are based on a three-layer *p*–*i*–*n* structure in which the *p*-layer and *n*-layer

are thin (a few microns) and the *i*-layer is approximately 200 μm. The *p*-layer (next to the substrate) is As_2Se_3 and the *n*-layer (between the *i*-layer and the positive electrode) is an alkaline-(Cs) doped $Se_{1-x}As_x$ ($x \approx 0.02$–0.05) alloy which is *n*-type [21, 22]. The thin layers act as "blocking layers" and reduce the dark current, but X-ray absorption and transport occurring in the *i*-layer dictate device performance; the work reported here is most relevant to that region. The work is aimed at improving our understanding of charge exchange processes within the band gap of stabilised a-Se (e.g. carrier trapping and recombination) and examining the role of valence alternation pair defects in these charge exchange processes.

Pulsed optical excitation was used to measure photocurrents in a frequency-resolved spectroscopic (FRS) mode and also the form of the individual photocurrent transients in the time domain. Our data reveal a complex picture for charge exchange during the light and dark phases of the FRS measurement. A striking feature of the overall transient response is the importance of a slow "recovery" period, during the light-off phase, which determines the form of the subsequent light-on transient and hence the FRS spectral shape. Spectral distortion in the lower frequency region is severe, and data in this region appear, at first glance, to lack consistency and reproducibility. However, by accounting for the kinetics of both fast and slow charge exchange over a wide frequency range, the observed behaviour is found to be both consistent and reproducible.

It is well established that a-Se contains a large number of defect states in the electronic band gap. In particular, a-Se has an "intrinsic" reservoir of bound and electrically charged defect states, valence alternation pairs (VAPs), which exist at the cross-linkage sites of the (predominantly twofold coordinated) Se atomic chains and dominate the material structure. The molecular orbital electronic configurations and ground-state energies of VAP defects have been described by Kastner et al. [23, 24] who established the link between coordination number and defect charge states and clarified the role of lone pair electrons in bonding configuration changes at the defect sites. Prior to this, Street and Mott [25] demonstrated that the same defects, labeled simply as dangling bonds, exhibited negative effective lone pair electron correlation energies (negative Hubbard energy U) due to lattice distortion following a change in charge state, helping to stabilise these gap states. This extended the concept of Anderson localization, based on polaronic lattice distortion [26], to point defects. The negative U property of VAPs has significant impact, pinning the Fermi energy in a-Se near mid-gap [24], ensuring that only two VAP defects exist stably in thermal equilibrium. VAP defect pairs can also exist in close proximity, in which case they are termed intimate VAPs (IVAPs). IVAPs can be formed from atoms on the same chain or from different chains; they can also exist in pairs [27, 28].

The two stable, singly charged, VAP defects form spontaneously in equilibrium as a net charge neutral pair, labelled C_3^+ and C_1^- [24], where C denotes the chalcogen (Se) atom at the defect site, the subscript is the coordination number for that atom, and the superscript is the defect charge state. The C_3^+ and C_1^- defects have no unpaired spins and therefore are EPR silent [29]. However, other singly charged and neutral VAP configurations exist which possess a net spin and so are, in principle, EPR active. The defect configurations C_3^0 and C_1^0 are metastable, but play a key role during the transformation between the stable states $C_1^- \leftrightarrow C_3^+$ under non-equilibrium conditions. The structure, electronic properties, and their photogeneration in a-Se have been analysed by atomic scale modelling [27, 28, 30]. Such approaches have linked a variety of optically active phenomena (e.g. photodarkening) with the structural and electronic changes promoted by optical pumping and also provided information on charge density distribution and electron binding energies [28].

In this work, we suggest that VAP defects, and particularly, the interconversion between the two stable VAP configurations can explain our experimental data without invoking any stable populations of the various neutral overcoordinated and hypervalent defects that have been proposed to exist [31]. Previous VAP-based interpretations of various electrical and optical properties of a-Se such as photoconductivity, post-transit time-of-flight (TOF) signals, photodarkening and interrupted field TOF have demonstrated the usefulness of VAP defect models [27, 29, 30, 32–39]. In fact a VAP defect-based model has been successfully used to explain the "ghosting" and the drop in sensitivity of a-Se photoconductors [40]. In some of this work, electron (hole) binding energies within the band gap have been suggested for VAP-based defects, although there is no generally agreed consensus on which VAPs or VAP complexes (including IVAP pairs) can be unambiguously assigned to these energy levels [38].

We have developed a model which ascribes many of the principal charge exchange and storage events observed in photoconductivity experiments to VAP defects. Our model is able to reproduce the very different optical responses observed in the high- and low-measurement frequency domains. The calculations reveal that, during optical excitation, strong hole trapping significantly modifies the electric field distribution in the near-surface region beneath the illuminated face of the solid. This field modification, in turn, changes both the balance of charge exchange, photogeneration and transport processes occurring in the near-surface region significantly beyond the optical extinction depth. By taking this into account we are able to explain what at first sight appear to be "anomalous" transient shapes and FRS data "distortion" at low frequencies. We have carried out electron paramagnetic resonance (EPR) measurements

down to low (4 K) cryogenic temperatures under intense laser light irradiation to test for the presence of light-induced spin active defects, but found no evidence for these.

2 Experimental procedure

Stabilised a-Se films of nominal thickness 100 μm were prepared by the vacuum evaporation of pre-alloyed a-Se: 0.3% As (doped with Cl in the ppm range) pellets from a molybdenum boat onto an Al-coated glass substrate in a conventional stainless steel vacuum deposition system. The substrate was heated and kept approximately at 65 °C during the deposition, which is known to result in high-quality a-Se films with good hole transport [41]. A semi-transparent circular gold electrode was used to complete a sandwich structure of Au/a-Se/Al. The photoexcitation was restricted to the central region of the Au electrode to avoid fringe field effects. The films were of electronic device quality and equivalent to the *i*-layer in a typical *p*–*i*–*n*-type a-Se X-ray detector structure. Charge transport and trapping in films of nearly identical composition and preparation conditions have been already extensively reported [41–43], and will not be repeated here, though parameters determined from similar time-of-flight transient photoconductivity measurements as in the latter references were used in the modelling the section below.

Frequency-resolved spectroscopic (FRS) measurements were performed using a 405 nm laser diode source for above optical gap (2 eV) excitation. In order to obtain a wide frequency range (from 0.1 up to 10^6 Hz), acousto-optic light modulation was employed. The Fermi level pinning close to mid-gap in a-Se results in low dark carrier concentrations and low dark conductivity. This necessitates the application of high dc voltages of typically 400 V across the a-Se layer of thickness of approximately 100 μm. The dark electric fields were, therefore, in the region of 4×10^6 V/m; however, we discuss below that during a light pulse the field profile rapidly becomes spatially non-uniform. Lock-in amplification was used for signal processing and to directly generate the FRS data; the lock-in reference and phase signals were set by light modulation. Closed cycle He cryogenics with high-stability temperature control was employed to vary the temperature of the sample, and single transient response was obtained using a digital oscilloscope together with a small current sampling resistor, averaging over typically several hundred transients for each measurement. Photocurrent transients were obtained using sandwich device structures, with front face illumination through semi-transparent surface gold electrodes. This geometry avoids coplanar electrodes which complicate data interpretation due to surface trapping as highlighted recently [44].

Electron paramagnetic resonance (EPR) measurements were carried out at the EPSRC UK National EPR Facility at the University of Manchester. The EPR measurements were performed using a Bruker EMXPlus spectrometer equipped with a ER4119SHQ resonator and a liquid He cryostat. The sample was sealed in a helium-filled quartz tube. The measurements were conducted at X-band (ca. 9.4 GHz) microwave frequencies, with 405 nm laser irradiation over a range of power densities from 0.1 to 10 W cm^{-2} and temperatures from 295 to 5 K. The measurements were also checked for reproducibility against standard samples of known spin characteristics, as well as with the known instrumental resolution of 5×10^{13} spins cm^{-3}. The background signal was recorded and subtracted for each single spectrum. No EPR signal above the background was observed from these a-Se films at any temperature, either in the dark or under laser illumination up to the highest power density used.

The absence of an EPR signal during laser irradiation was unexpected given the previous reported spin detection in laser irradiated a-Se at low temperatures [29]. In the latter work, the illumination was from an Ar laser at 514.5 nm (absorption depth of ~ 0.1 μm) with a light intensity of 50 mW cm^{-2}. Our measurements used 405 nm excitation (absorption depth of ~ 0.05 μm) and a power density spanning a range greater than that used in [29]. There are some differences in sample properties: while a pure a-Se film was used (with no substrate deposition temperature information) in [29], our sample is stabilised a-Se (0.3% As with ppm Cl) and deposited at a substrate temperature above the glass transition temperature. The latter deposition condition is known to yield films of high electronic quality (with low concentration of deep hole traps).

3 Frequency-resolved spectroscopy

Typical FRS data sets, shown in Figs. 1 and 2, were recorded over six orders of optical excitation frequency and illustrate, respectively, the effects of changing the bias levels and light excitation intensities. The data in these figures are for three similarly fabricated samples (S1, S2 and S3). Other samples exhibited similar behaviour, but in general we observed slight variation in peak value from sample to sample. These data raise some specific questions concerning the form of the transients sampled by the FRS method during "light-on" and "light-off" phases. From both figures, it is clear that the low-frequency region of the spectra do not conform to the expected square wave response which would signify a typical flat "in-phase" (*X*) signal and a corresponding zero quadrature signal (*Y*). This observation indicates that the transient photocurrent response to a square light pulse at low frequency (i.e. a "slow measurement time window") does not follow the
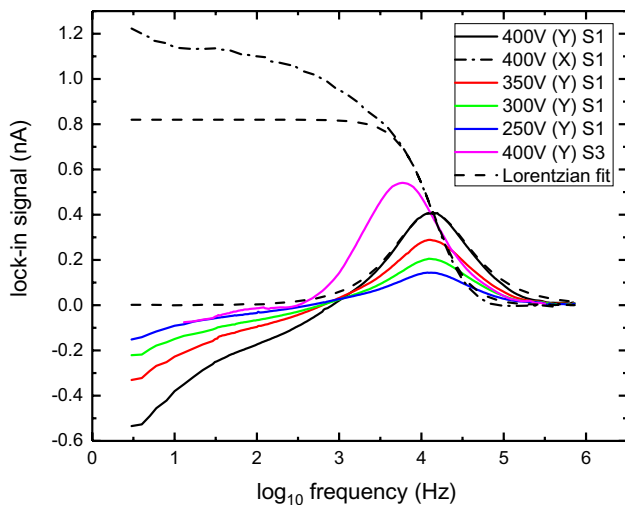
Fig. 1 Typical FRS spectra measured using a 405 nm laser diode, with different positive biases applied to the light-receiving surface of a-Se samples S1 and S3. Both in-phase X and quadrature Y (coloured continuous curves) components are shown for the 400 V spectrum from S1, for the other voltages, and for S3, only the Y-component is shown (which contains spectral content). The dashed line is a fit to the 400 V S1 spectrum using a pure exponential (rise and decay) with time constant 12.1 μs. The S3 peak corresponds to an exponential time constant of 41.9 μs. The measurements were performed at room temperature
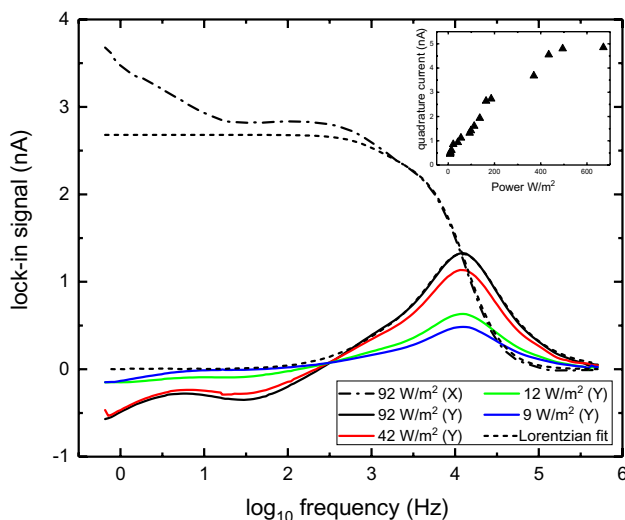

Fig. 2 FRS spectra recorded on sample S2, for four different light intensities, with 400 V (positive) applied to the top (light-receiving) surface of the sample, are shown. The quadrature (Y-component) signal is shown for all light intensities; the X-component (dash-dot, in-phase component) of the signal is only shown for the highest intensity of light. The dotted lines show the expected X and Y signals for a 2-component exponential decay with time constants 11.6 μs (88% of the signal) and 130 μs (12%). The inset shows how Y maximum varies with light intensity, at wavelength 405 nm

excitation profile. Instead, the in-phase component shows a steep decline with increasing frequency, and the quadrature component is negative.

As the frequency is increased, more conventional FRS spectra are observed, with the peak in the quadrature signal crossing the in-phase signal at the point of inflexion. This indicates that the photocurrent transients, at high frequencies, do conform to a simple exponential form, with similar rate characteristics for both the rise and the decay. The natural line shape for FRS Y spectra which results from sampling such symmetrical exponential rise and decay transients is Lorentzian, with characteristic exponential rise and decay time $1/(2\pi f_{max})$. Figures 1 and 2 record data from three different samples; samples 1 and 3 (Fig. 1) show a time response at high frequency which can be approximated by a Lorentzian fit resulting from single exponentials, with time constants 12.1 μs and 41.9 μs, respectively (using an experimentally determined pre-factor). The time response for sample 2 (Fig. 2) is characterised by two-component exponential rise and decay times, with time constants 11.6 μs (accounting for 88% of the decay magnitude) and 130 μs (12% of the decay). The shoulder on the FRS spectra in Fig. 2 confirms that two processes are involved in the rise and decay events. While some variation is observed in the time response from these films, they exhibit the same general trends, with the dominant processes over the measured frequency range being broadly similar.

The magnitude of the Y-signal peak varies with both voltage, Fig. 1 and light intensity, Fig. 2, but the frequency of the peak, f_{max}, remains relatively constant for each sample (it was found to vary from sample to sample as mentioned above). This absence of any electric field dependence of the peak frequency f_{max} suggests that neither the photocurrent rise nor the decay rates are controlled by the hole transport rate across the sample, i.e. by the transit time. In this case, kinetic control must be associated with some other time-dependent charge control process and exchange process at defects is an important candidate.

At lower measurement frequencies, Figs. 1 and 2 demonstrate that the photocurrent transients exhibit severe distortion: the fit to the model, Lorentzian, spectrum generated using simple exponential transients is poor for both X and Y components over this frequency range. Some additional and slower current controlling mechanism becomes active at low frequencies which does not control the response at high frequencies. These processes are not immediately discernible from the shape of the FRS spectra, but could be linked to some intrinsic property of a defect system. For these reasons, it is important to understand the individual transient responses and to identify experimental conditions which have influence on the form of these transients, to help build a physical picture of the dynamic processes occurring within these measurements.

4 Single photocurrent transients

Individual photocurrent transients, including both the rise and decay, are shown in Fig. 3. The transients shown were averaged over a long train of light excitation pulses, typically several hundred periods. It is a common observation for a-Se that slow changes can be triggered by the application of light or voltage excitation [45, 46]. Some stabilisation time is, therefore, necessary in order to yield highly reproducible transients and this was allowed for all data reported here. The individual transients shown in Fig. 3 explore the effects of varying the length of the dark time, between light pulses, for a fixed light pulse duration of 0.5 ms and a fixed positive bias of 500 V applied to the illuminated surface. It is observed that varying *only* the dark time between light pulses has a profound effect on the form of the "light-on" transient; for the data shown in Fig. 3, the dark rest time varied between 0.5 ms and 509 ms, over three orders of magnitude. This includes lengthening of the dark time beyond the time taken for the photocurrent transient to have completely decayed. We note that there is generally a small, but reproducible persistent increase in the value of the dark current for longer dark times.

In the case of the shortest dark time shown (500 µs), a simple exponential rise and decay are observed, consistent with the high-frequency FRS spectral shape. For this short dark recovery time, the transient amplitude is small. The obvious effects of lengthening the dark time are twofold:
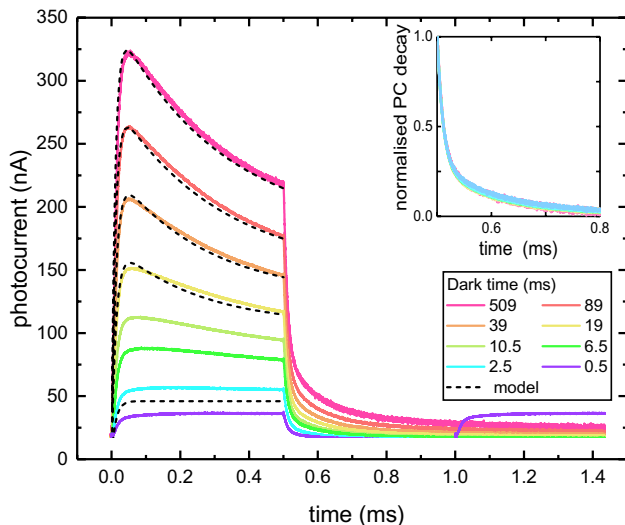
firstly, an increase in the magnitude of the photocurrent and secondly, and most dramatically, a change in shape of the photocurrent transient during the light pulse viz. the development of an 'overshoot', with amplitude also strongly dependent on the length of the dark time.

The evolution of transient shape in Fig. 3 explains the low-frequency form of the FRS spectra: a frequency-dependent overshoot, whose magnitude increases at low frequencies (longer dark times), would produce both the steep decline of the X-component and also the negative sign of the Y-component. As the FRS measurement frequency is increased, the square wave signal processing nature of lock-in detection dictates that dark time is reduced. The reduced dark time in the higher frequency domain is the necessary condition for suppression of the overshoot; the resulting exponential photocurrent rise/decay is clearly seen for the shortest dark time (500 µs) shown in Fig. 3. The inset in Fig. 3 shows the normalised post-optical-pulse transients and demonstrates that these vary only in magnitude and that the photocurrent decay rate, *for fixed bias and light pulse duration*, is independent of the length of the dark time. The marked effect of the dark period on the "light-on" photocurrent transient provides important insight to the nature of the charge exchange processes driven by the light excitation and underscores that it is the balance of the light-on and light-off times that controls many features of the photocurrent transient shape.

We stress that it is the length of the dark recovery time well beyond the end of the recorded transient decay which determines the amplitude and shape of the subsequent photocurrent transient. It seems likely that slow reorganisation of bonding configuration, perhaps with associated charge adjustment, occurs in this dark period. However, these internal changes have only a very small effect on the measured dark current. Such slow "recovery" processes, linked to configurational changes at defects, are a known feature of VAP centres in chalcogenide glasses [47].

The results of fitting the measured photocurrent light-off transients from one of the samples (S2) to two-component exponential decays are shown in Fig. 4 for which a wide range of "light-on" pulse lengths were used to obtain data, with a fixed dark time of 0.5 ms. The time constants obtained for three bias voltages are plotted as a function of light pulse duration in Fig. 4.

The decay was found to be double exponential in nature with fast and slow components,

$$i_{ph}(t) = A_1 \exp(-t/\tau_1) + A_2 \exp(-t/\tau_2) \tag{1}$$

where A_1 and A_2 are the pre-exponential constants and τ_1 and τ_2 are the decay time constants. The rates in Fig. 4 correspond to $1/\tau_1$ (fast) and $1/\tau_2$ (slow) decay rates. In all cases, A_1 is about 85–90% of the whole decay $(A_1 + A_2)$. The sample S2 used to provide the data for Fig. 4 is that used to

Fig. 3 Single photocurrent transients measured, at room temperature, from sample S2, with varying the dark time between successive 500 µs light pulses and with an applied bias of 500 V. The effect on transient amplitude and shape of varying the dark time delay time is shown. Inset shows normalised decay transients for all dark times plotted, illustrating no dependence on the dark time
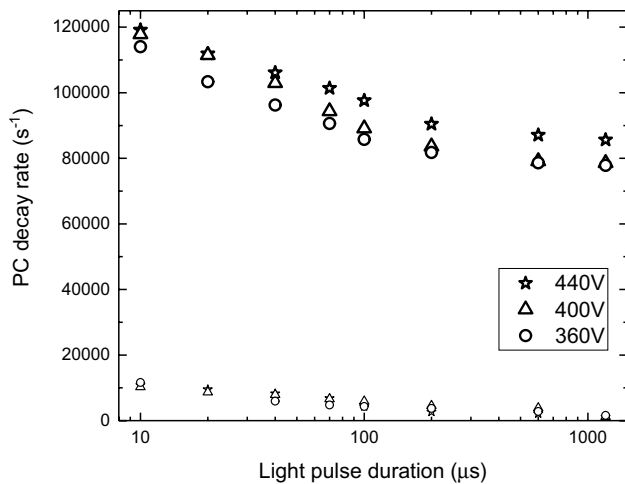
Fig. 4 The effect of light pulse duration on the rate of the post-optical pulse photocurrent decay in one of the samples (S2), rates determined by fitting the decay to Eq. (1). The upper points correspond to the fast decay rate $1/\tau_1$ and the lower points to the slow decay rate $1/\tau_2$. The dark time was kept constant at 100 ms for all measurements. The fitted rates are shown for three different biases applied to the top electrode. In all cases, the faster decay (A_1) comprises of 85–90% of the total decay magnitude, and the slower decay A_2 comprises of 10–15% of total decay magnitude

Fig. 5 Arrhenius plot of the high-frequency quadrature FRS peak (triangles) measured on sample S3. The inset shows some of the normalised FRS peaks measured at different temperatures. Dash-dot line shows how the modelled photocurrent decay rate varies as a function of temperature (The model is described in Sect. 6)

obtain the FRS spectra shown in Fig. 2, which also pointed to the presence of two rate processes. The rate constants and fractional contributions inferred from the FRS spectra agree well with the numbers obtained from analysing the decay constants.

This more detailed approach does reveal a very a small dependence of the decay rate on the applied bias, not discernible from the spectral peak position in Fig. 1; however, the most significant change in the decay rate is observed for different optical pulse durations: the shorter the optical pulse, the faster the photocurrent decay. This is discussed further in Sect. 6. No dependence of decay rate on dark time was observed.

5 Thermal activation

The effect of temperature on the rate constants was investigated using high-frequency FRS data; the results are shown in Fig. 5. These data were recorded using sample S3, for which a room temperature FRS spectrum is given in Fig. 1; the characteristic room temperature rate constant for this sample was measured to be 41.9 µs. The change in the rate constant with temperature can be determined from the shift of the high-frequency peak of the quadrature signal in the FRS spectra ($1/2\pi f_{max}$). The measurements were made with a positive potential of 400 V applied to the electrode on the photoexcited surface. As the temperature is reduced from
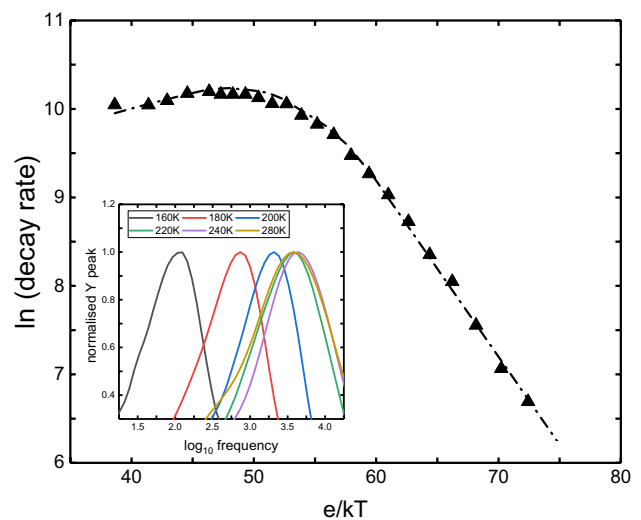
295 K, an initial *rate increase* is observed, i.e. a change in the *opposite* sense to that expected from Arrhenius activation (Fig. 5). This trend continues until approximately 240 K is reached, when the rate is a maximum. These data demonstrate that the processes giving rise to the transients, measured at room temperature (where FRS data and single transients were obtained), do not show Arrhenius activation. Only when temperature is significantly reduced (to below 240 K) does Arrhenius behaviour emerge.

It is clear then that the mechanism(s) controlling the high-frequency current transients at temperatures close to room temperature are not associated with thermally activated charge release from gap states; that process alone would continue to show strong activation at and near room temperature. However, when the temperature drops significantly below room temperature, the rate constant does become thermally activated with an activation energy of around 0.2 eV; this compares well with the typical *effective energy* of shallow traps that control hole transport in a-Se (over the same temperature range) [38]. In this low-temperature regime, therefore, the photocurrent decay process is likely to be limited by the hole mobility.

Close to and at room temperature, some other mechanism for current control is required to explain the change in the sign of thermal activation. Clearly, at these higher temperatures, the dwell time (release time) of a hole in a shallow trap is reduced. This, together with the lack of voltage dependence, argues against transport limiting the photocurrent transient. Reported hole mobility data for a-Se would, at the electric field values employed, give rise to fast photocurrent

(sub-microsecond) decay times. Of the known rate constants for transient current flow in a-Se, only that associated with hole lifetimes are of the order of 10–100 µs [38, 48], similar to the time scales reported above.

6 Modelling charge exchange and electric field distortion

6.1 Overview of the VAP-based model

The objective of the model in this work is to quantify our understanding of the way in which the dark/light times control the shape of photocurrent transients and, equally, the marked change in charge exchange kinetics near room temperature revealed by the non-Arrhenius temperature dependence. Such a model must account for charge storage (trapping) and recombination. It must also account for any associated electric field change which, in addition to trapping and recombination, can influence current flow. We show that many features of the FRS data can be successfully reproduced if a high concentration of sub-surface positive charge is allowed to build during a light pulse, with subsequent slow charge relaxation (recovery) effect during the following dark period.

The fundamental assumption of the model in this work is the existence of charged under- and over-coordinated VAP defects, C_1^- and C_3^+, which may include their derivatives or combinations [28]. The structure is considered to be charge neutral before non-equilibrium experimental conditions are established. The model assigns the primary, positive, charge trapping process as a light-induced conversion of C_1^- to C_3^+, i.e. $C_1^- + 2h^+ \rightarrow C_3^+$. We have assumed that the C_3^+ and C_1^- defects involved (formed at separate Se chains) are effectively isolated, in the sense that electron transfer between defect sites does not occur. Also, the inclusion of a light-generated population of C_3^+ defects, with a spatial (depth) profile similar to the extinction depth of the exciting light, was found to be crucial in order to successfully model our data. Thus, the model is built on a combination of direct light generation of charge neutral pairs (VAPs) followed by $C_1^- \rightarrow C_3^+$ conversion. We have modelled the "back conversion" in the dark as sequential capture of electrons into the charge-unbalanced population of C_3^+ defects, i.e. $C_3^+ + 2e^- \rightarrow C_1^-$.

Trapping and release of carriers from shallow electron and hole traps, not necessarily ascribed to VAP species, are included in the model. The shallow traps maybe excited states of VAP defects or simply a derivative of a VAP defect [38]. Further, the transport effect of a sharply decreasing distribution of localised states from the transport band edge to some depth ΔE would appear as though there is an effective level of shallow traps located at ΔE. The inclusion of

shallow traps allowed us to discriminate at any specific time between the fraction of electrons/holes which contribute freely to transport (with a "band mobility") and those dwelling in traps. We assume it is this free carrier population which can partake in recombination. Electron–hole recombination has been modelled with IVAPs providing the recombination channel; this notion has been reviewed for chalcogenide glasses by Shimakawa et al. [49]. The close proximity of the IVAP components allows us to approximate them as single, polarised, "pair defects": they were not allowed to store charge in the model, only to facilitate sequential hole-electron capture. It should be acknowledged that this choice probably represents a subset of the total IVAP population for which charge separation is sufficiently small (this is discussed further in Sect. 7). The assumption on the one hand of effectively isolated C_3^+ and C_1^- defects for charge storage, and on the other hand, of closely coupled C_3^+ and C_1^- defects in IVAPs for recombination, is important in the model and is also convenient. Such a distinction was noted by Adler and Yoffa [23] who pointed out that for isolated species one can neglect any Coulomb interaction energy in the total energy of the defect. Electron and hole capture processes are critical for this work and the choice of appropriate values for capture rate coefficients is, therefore, important; more detail on the model parameterisation is given in the next two sub-sections.

The importance of near-surface positive charge storage in the model is its effect on the local electric field profile and band curvature, reducing the near-surface field strength and locally flattening the energy bands. These effects exert a major influence on the current flow and ultimately on the form of photocurrent transient. The reason for the field perturbation is that although the integrated positive charge in the system (contacts plus bulk sample) remains constant, the build-up of stored positive sub-surface charge results in a reduction in the sheet charge density on the top metal contact. In the limit of significant charge storage in the sample, the field profile in the sub-surface region is dictated by the volume density of positive charge in the defect states. Under the constant voltage conditions used, the low field near the surface is compensated by a small increase in field strength in the remaining sample.

Owing to the near insulating properties of a-Se, characterisation methods almost exclusively use high electric field conditions. The outcomes of the model presented here suggest that the low-field conditions, albeit confined to a small region below the surface, dominate the transient photocurrent response. In this region, the build-up of optically injected carrier densities become controlled by the local carrier lifetime. The photocurrent can be thought of as being driven by the extraction of holes from the low-field zone. The *limitation* on the magnitude of the photocurrent, however, is determined by the *supply* of photogenerated holes from the low-field region, and the diffusion and/or drift of these holes to the high field

region for extraction. The recombination lifetime for the photogenerated electron and hole population in the near-surface region becomes the controlling factor in the current decay. This situation is illustrated schematically in Fig. 6.

6.2 The physical model and numerical algorithm

Rate equations were established to account for the evolution and movement of charge carriers during light excitation i.e. the information required to map the solution of Poisson's equation in time, allowing one to calculate the instantaneous electric fields and band bending needed to compute transient current flow. The overall goal is to test if charge transfer properties connected with valence alternation defects can explain our data. Specifically, we wanted to test if (near-surface) positive charge, stored in excess C_3^+ defects during the start of each light excitation pulse, but decaying during the dark period, gives rise to the measured transient distortion. The rate equations used are given in Eqs. (3) and (4), together with the associated form of Poisson's equation (2). The rate equations account for charge continuity: electron and hole generation, recombination, capture, release and movement (current divergence). Their parameterisation includes both VAP defects and shallow electron/hole traps, and their solutions for time t provide the instantaneous spatial charge profiles needed to populate the Poisson equation (2). In one-dimensional geometry (neglecting variations in the lateral y and z directions), the Poisson and rate equations are

$$\frac{\partial^2 \varphi}{\partial x^2} = -\frac{q}{\varepsilon_s}\left(N_{vap}^+ - N_{vap}^- + N_h^+ - N_e^- + p - n\right) \tag{2}$$

$$\frac{\partial p}{\partial t} = G + A_h N_v N_h^+ e^{-E_h/kT} - A_h p(N_h - N_h^+)$$
$$- A_{vap}^- p N_{vap}^- - A_{ivap} p N_{ivap} + \frac{\partial}{\partial x}J_p \tag{4}$$

where x is measured from the light-receiving electrode towards the rear electrode, φ is the local instantaneous potential $\varphi(x,t)$, $p = p(x,t)$ and $n = n(x,t)$ are the local instantaneous (spatially distributed) free hole and electron concentrations, q is the elementary charge, ε_s is the dielectric permittivity of the semiconductor ($\varepsilon_0\varepsilon_r$), J_p and J_n are the local hole and electron current densities, G refers to the optical generation rate, which includes the temperature and field dependence of the photogeneration efficiency based on [50] (rather than the more complicated full Onsager expression), N_{vap}^+ and N_{vap}^- are the local concentrations of the singly charged, isolated, VAP defects C_3^+ and C_1^-, N_h/N_h^+ and N_e/N_e^- represent the total/ionised concentrations of shallow hole and electron traps, while E_h and E_e are the effective depths of these shallow traps from the respective transport band edges. N_{ivap} and N_{vap}^+ are the local concentrations of overall neutral and (transiently) positively charged IVAPs which together act as the recombination channel. The rate coefficients for each process are labelled A with the subscript denoting the process and are discussed in detail in the next section. Other symbols have their usual meanings.

A numerical algorithm was developed for solving the set of Eqs. (2) to (4). The initial dark conditions are determined assuming $\partial n/\partial t = \partial p/\partial t = 0$ and by solution of Poisson's equation using dark values for the fixed charge density at VAP and shallow trap sites. Most notably, the initial

$$\frac{\partial n}{\partial t} = G + A_e N_c N_e^- e^{-E_e/kT} - A_e n(N_e - N_e^-) + A_{vap}^- p N_{vap}^- - 2A_{vap}^+ n N_{vap}^+ - A_{ivap}^+ n N_{ivap}^+ + \frac{\partial}{\partial x}J_n$$
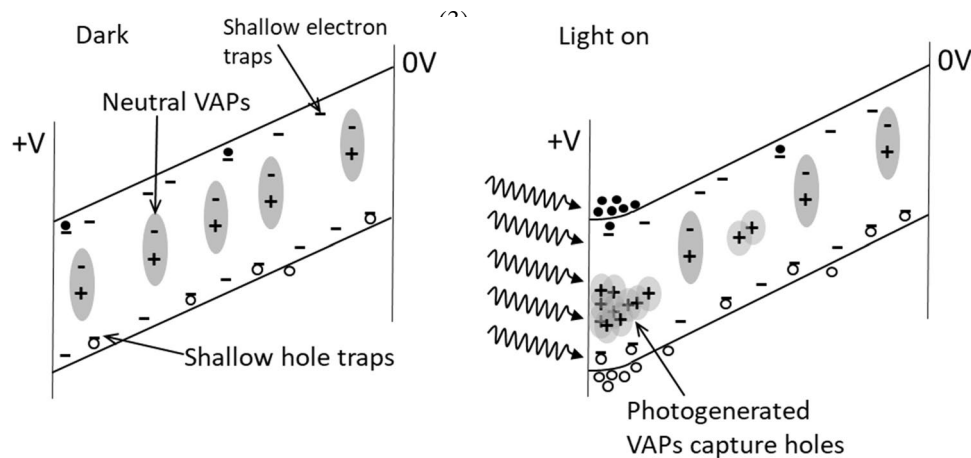
(3)

Fig. 6 A schematic illustration showing the band diagrams and voltage distributions before (left) photoexcitation and during (right) a light pulse. Photogeneration and charging of VAPs is illustrated, together with the effect the sub-surface charge has on the voltage profile. The degree of near-surface band flattening depends on the local charge density; the flat band profile depicted here requiring $\rho^+ \sim 5 \times 10^{15}$ cm^{-3} for an exponential charge depth profile with extinction depth 0.2 µm with an applied voltage of 400 V

condition has no excess positive (or negative) trapped charge. The initial band bending determined for samples with no prior illumination history then resembles the tilted bands depicted on the left in Fig. 6. A light excitation cycle was then invoked with switch-on at $t = 0$ and switch-off at $t = 1/(2f)$, where f is the modulation frequency of the light source. The rate equations describe the evolution and movement of charge during light excitation; they contain several terms, all space (x) and time (t) dependent. The numerical procedure adopted for their solution was based on rate equation linearization (Euler's method). With this method, high precision is required in order to compute the finely varying local derivatives; hence time intervals δt of typically 10^{-10} s were used: δt was sufficiently short to ensure that the rate equations were at all times dealing with small changes in charge concentration, ensuring good time resolution represented the main computational overhead.

For any specific t, the calculation determined charge exchange and movement at, typically, 1000 values of x. These were non-linearly spaced so that a higher resolution could be achieved in the critical light absorbing region. The spatial information on fixed and mobile charge was passed into Poisson's equation which was then solved numerically using Newton's method; the fixed potential difference between the front and back surfaces formed the boundary conditions for this calculation ($\varphi(0,t) =$ applied voltage V at $x = 0$ and $\varphi(L,t) = 0$ at $x = L$, the sample thickness). With the potential and charge distributions now obtained for this t, the value of electron and hole photocurrent contributions J_n and J_p was obtained from the usual expression for drift and diffusion. These values of J provide a point on the photocurrent transient corresponding to the time t. The total number of successive time intervals δt was sufficient to ensure that a complete transient could be obtained, so a total time longer than the excitation cycle time was used, typically $t = 5/f$. This choice of total time was made in order to ensure that the correct conditions for a repeatable cycle had been established.

6.3 Assignment of rate coefficients

For the VAP-related events, the assignment of rate coefficients is complicated by the problem that the stable charge conversion of defects involves multiple steps. In the present model, this issue was dealt with using the fact that the dynamic processes, which emerge from molecular orbital discussions, identify rate-limiting steps for valence alternation charge exchange sequences. This allowed us to use a single rate coefficient for each sequence. We note that the charged VAP states, C_1^- and C_3^+ in the continuity/rate equations, (3) and (4), could in principle also be associated with As atoms in the dilute alloy materials used here, arising from

under- and over-coordinated As atoms (As_2^- and As_4^+) in the chains and cross linking chains. Our model does not distinguish between different chemical species of a VAP defect. However, the energy cost of forming under- and over-coordinated As defects is expected to be somewhat greater than for that of a chalcogen atom and so there is some justification for assuming that it is probably the Se-related defect species which undergo charge conversion.

For hole capture associated with the positive charging in the region of the sample directly excited by light, the calculation assumes that a spatially decaying profile of VAPs is produced on a time scale which is fast compared to the measurement time scale. The charge build-up then corresponds to the conversion $C_1^- \rightarrow C_3^+$ through an initial capture of a hole followed almost immediately by valence reconfiguration and subsequent electron emission (or a second hole capture). Each of these steps must have a characteristic time. Since atomic reorganisation followed by the emission of an anti-bonding electron are expected to occur quickly (Sect. 7), we identify hole capture to be the rate-limiting step. For these reasons, the double charge exchange is accounted for by the single rate coefficient A_{vap}^- and the term $A_{vap}^- p N_{vap}^-$ appears in the equations for both $\partial p/\partial t$ (hole capture) and $\partial n/\partial t$ (electron release).

In semiconductors with high carrier mobility, electron and hole capture at point defects is frequently described by Shockley–Read–Hall (SRH) kinetics [51]: the incoming carrier is considered to have ballistic motion and, in large part, the energy loss mechanisms dictate the size of a capture cross section, σ. However, for low-mobility materials, the rate at which carriers can diffuse to a sink may limit the overall capture rate. In such a case, the incoming particles are not ballistic instead they execute a diffusive motion down a local potential gradient towards the capture site. Diffusion rate-limited capture is often described by the Langevin model [52] which treats capture at a singly charged, Coulomb attractive defects. The probability of thermal escape from a Coulomb potential is implicit in the value of the Langevin rate coefficient: $q\mu/\varepsilon_s$, which in the present case has the value $A_{vap}^- = 2.8 \times 10^{-7}$ cm^3 s^{-1}. This value was determined using a (band) hole mobility of $\mu_h = 1$ cm^2 Vs^{-1} [53]; the measured drift mobility value for a-Se was not used here as it factors in time spent in the shallow traps and the value of p used in Eq. (3) refers to the density of free holes in the valence band at time t.

Double (sequential) electron capture into C_3^+, sourced from the dark current, was used to model the $C_3^+ \rightarrow C_1^-$ back conversion both during optical excitation and in the dark phase. The back conversion rate is likely to be endothermic [24], it would, therefore, be rather slow and contribute very little to measurements which involve short dark times. It does, however, exert a major influence on low-frequency

FRS spectra and single transients which include long dark times. Simply assigning a Langevin coefficient to the first electron capture step at the Coulomb attractive C_3^+ site producing the C_3^0 defect would be inappropriate because of the instability of C_3^0 which energetically favours a rapid return to the C_3^+ state. Such instability in capture mirrors, for example, the reduction of an SRH capture rate when the initial stage of capture is into a thermally unstable excited state rather than directly into the ground state [54]. Consequently, we assigned a much lower number for this rate coefficient: $A_{vap}^+ \sim 10^{-13}$ cm^{-3} s^{-1}, with this single coefficient parameterising the double electron capture process in the term, $-2A_{vap}^+ n N_{vap}^+$.

The rate coefficients in Eqs. (3) and (4) connected with electron–hole recombination in the low-field region, A_{vap}^- and A_{vap}^+, determine, respectively, the rate of hole capture at the net charge neutral IVAP defect, and the rate of subsequent electron capture at the resulting positively charged system. Aside from the small time interval associated with the sequential hole and electron capture events constituting recombination, the IVAPs were constrained to retain their stable (dipole) charge neutral configuration: like any defect recombination centre, no charge is stored by the IVAP pair. Since we modelled hole capture as a charge neutral event, a Langevin rate coefficient was not used (the IVAP field is not Coulombic). Rather an SRH cross section, $\sigma_{ivap} \approx 1 \times 10^{-15}$ cm^2, was assumed (at room temperature), with a corresponding rate constant $A_{ivap} = v_{th}\sigma_{ivap} = 1 \times 10^{-8}$ cm^3 s^{-1} in Eq. (3). At very close distances though, the hole will experience interaction with the short range dipole field of the IVAP. Short range effects were considered by Lax [54] who treated the effect of polarisation of neutral point defects by the incoming particle. In the present case, polarisation is intrinsic to the charge organisation of the IVAP and the long range attractive component of the dipole field, $E(r) \sim (1/r^3)$, will aid hole capture. However, the temperature variation of σ (and hence the rate coefficient) is likely to be associated with the stronger short range dipole field. We have assumed that thermalisation competes with capture for the first particle capture event at the IVAP and that a temperature power law applies similar to that often measured for capture at attractive centres. In the model, we have assigned a variation of T^{-2} to σ_{ivap} and hence a temperature variation of $T^{-1.5}$ to A_{ivap}.

The recombination process is completed by electron capture into the now Coulomb attractive defect and assigned N_{ivap}^+ a Langevin rate coefficient $= A_{ivap}^+ = 2.8 \times 10^{-7}$ cm^3 s^{-1}, (assuming a band mobility of 1 cm^2 Vs^{-1}); this is significantly larger than A_{ivap} in Eq. (4). Unlike the double charge transfer associated with trapping and relaxation at isolated VAPs considered above, IVAP recombination was implicitly treated as two distinct processes, each requiring a rate coefficient. We suggest that valence configurational changes are *transiently* involved in the full IVAP recombination sequence and do not limit either rate process, but may play an important role in stabilising the IVAPs as recombination centres during the transient event; this is discussed in more detail in Sect. 7.

The shallow traps were assumed to be charge neutral before capture. Capture events are assigned the rate coefficients A_h and A_e, respectively, for hole and electron traps in Eqs. (3) and (4), and SRH capture at charge neutral defects was used in the model. Capture cross sections σ in the range 10^{-17}–10^{-15} cm^2, usually linked with neutral capture, and were tested. Optimisation was achieved for $\sigma = 5 \times 10^{-16}$ cm^2 for both types of trap and so the corresponding rate coefficients: $A_e = A_h = 5 \times 10^{-9}$ cm^3 s^{-1} were used in the model. The emission rate coefficients for these shallow traps are linked to their respective capture coefficients through detailed balance using the particle binding energies, E_h and E_e. The effect of shallow traps would remain the same if we were to assume charged shallow traps, but instead use a lower concentration so that their product remains the same.

6.4 Model predictions

It became clear from our initial attempts at modelling the experimental data that in order to reproduce the shape of the measured transients, (i) efficient positive charge storage in the sub-surface was important, (ii) positive charge must increase significantly during direct light excitation, and (iii) the stored charge must relax back slowly over time in the dark. These attributes, are known to be characteristic of VAPs [35, 49]. The calculated transients are compared directly with the experimental data of Fig. 3, where the model outputs are given by the dashed lines. The values assigned to all parameters which best succeeded in matching the data are summarised in Table 1. Since the rate equations contain a number of variables, it is useful to comment on the sensitivity of the fit to the values used for these parameters. Many of the values used (e.g. "band" mobility, shallow trap energy depth and relative permittivity) are typical for a-Se and were considered to be fixed. Rate coefficients were chosen to be consistent with Langevin or SRH capture for either charged or neutral defects as appropriate. The concentrations of both shallow traps and VAPs are not accurately known and were varied here, within plausible limits, to improve the fit. In terms of fitting the detail of the shape of the transient overshoot, it was discovered that the charge density remaining in the VAP population following each dark period was the most sensitive fitting parameter.

The simulation confirms that transient overshoot is consistent with field modification near to the surface, and allows us to understand these transients in the following way. During long (experimental) dark times, any net stored charge

Table 1 List of parameter values used in the model

Parameter	Physical properties	Assigned value(s) at room temperature
N_{vap}^+, N_{vap}^-	Concentration of singly charged VAP defects	Surface (uncharged) population: $N_{vap}^+ = N_{vap}^- = 3.5 \times 10^{15}$ cm^{-3}. Exponential depth profile due to photogeneration, decay length 0.2 µm; bulk concentration $= 1 \times 10^{12}$ cm^{-3}
N_e, N_h	Concentration of shallow electron and hole traps	$N_e = N_h = 2 \times 10^{15}$ cm^{-3} (lower values can be used if the capture cross section below is increased)
E_e, E_h	Energy of shallow traps relative to their associated band edges	Electron traps: 0.32 eV Hole traps: 0.2 eV
A_{vap}^-	Langevin rate coefficient for $C_1^- \to C_3^+$ conversion (rate-limiting process considered to be hole capture)	$A_{vap}^- = 2.8 \times 10^{-7}$ cm^3 s^{-1}
A_{vap}^+	Rate coefficient for the complete $C_3^+ \to C_1^-$ dark charge recovery process (electron capture)	$A_{vap}^+ \approx 10^{-13}$ cm^3 s^{-1}
N_{ivap}	Concentration of neutral recombination centres (considered to be subset of IVAP pairs)	$N_{ivap} = 7.7 \times 10^{12}$ cm^{-3}
A_e, A_h	Rate coefficients for electron (hole) capture into (empty) shallow electron (hole) traps	$A_e = A_h = 5 \times 10^{-9}$ cm^3 s^{-1} cross section, $\sigma = 5 \times 10^{-16}$ cm^2
A_{ivap}	Rate coefficient for hole capture into (overall) charge neutral IVAP, N_{ivap}	$A_{ivap} = 1 \times 10^{-8}$ cm^3 s^{-1} cross section, $\sigma = 1 \times 10^{-15}$ cm^2
A_{ivap}^+	Langevin Rate coefficient for Coulomb attractive electron capture at the C_3^+ IVAP component, N_{ivap}^+	$A_{ivap}^+ = 2.8 \times 10^{-7}$ cm^3 s^{-1}
μ_e, μ_h	Electron, hole "band" mobility	$\mu_e = \mu_h = 1$ cm^2 Vs^{-1}
ε_s	Permittivity of a-Se	$6.5\varepsilon_0$ ($\varepsilon_0 =$ absolute permittivity)

that exists in the near-surface VAP population (excess C_3^+) relaxes closer to the equilibrium charge-balanced population, so that when the next optical pulse arrives, the bands are fully tilted at the interface (Fig. 6, left). Both types of carrier are rapidly extracted, electrons being removed to the top electrode and holes driven into the bulk of the solid towards the rear electrode. These processes produce a large rate of initial increase in current and large current amplitude. However, as the photocurrent transient (and VAP photogeneration) proceeds, hole trapping into the C_1^- population occurs. This results in positive charge storage. As the positive charge density ρ^+ increases, so does the effective screening of the surface field and associated flattening of the bands (Fig. 6, right). The latter processes reduce the drift current and an overshoot results, with the measured current dropping to the value of the smaller, steady-sate, hole extraction current.

For the calculated transients in Fig. 3, the surface concentration of VAPs was assumed to have the value 3.5×10^{15} cm^{-3}. The various transients were calculated by assuming different initial (exponential) positive charge density near the surface at $t = 0$. For the (longest) modelled dark time of 509 ms, the surface concentration of VAPs was assumed to be $N_{vap}^+ = N_{vap}^- = 3.5 \times 10^{15}$ cm^{-3}, i.e. zero stored charge at the start of the transient. For the modelled curves associated with the 89 ms, 39 ms, and 19 ms dark times, respectively, initial N_{vap}^+ concentrations of 3.92×10^{15} cm^{-3}, 4.31×10^{15} cm^{-3}, and 4.69×10^{15} cm^{-3} provided the best fit

(together with the correspondingly lower concentrations of N_{vap}^-); the transient calculated for a fully charged VAP (N_{vap}^+) population is also shown.

Our simulations confirm the necessity of including VAP photogeneration and the resulting enhanced positive charge storage in the sub-surface: a decaying exponential for the depth profiles of N_{vap}^+ and N_{vap}^- was needed for good agreement between the model and experiment. If charge storage were to result from hole trapping at a uniform defect distribution, then trapping would occur throughout the film thickness, resulting in an extensively distributed ρ^+ profile. Such a charge profile would not yield the measured overshoot and field-independent FRS signal. An optimised characteristic decay depth of 0.2 µm was used for this exponential VAP profile. This is somewhat greater than the expected (low field) optical extinction depth (0.05 µm for 405 nm light). However, a build-up of injected carrier density beyond the region of light penetration is probable due to the carrier diffusion. In fitting these transients, it was found to be important to include electron trapping at shallow traps. This process reduces the large electron current which would otherwise result from extraction of electrons to the nearby top contact in conditions of a strong field. The concentration of shallow traps was set to $N_h = N_e = 2 \times 10^{15}$ cm^{-3}. The hole/electron shallow trap energies were assumed to be 0.2 eV/0.32 eV from the respective band edges and these values were not adjusted (it is possible to make the same fit

by decreasing the shallow trap concentration and increasing the capture cross section, as mentioned previously).

The screening effect described can be used to understand several experimental observations: the different rates of increase seen in the photocurrent after different dark times (Fig. 3) can be explained in terms of the different amounts of positive charge remaining at the end of the dark time. The dependence of the decay rate on the light pulse duration (Fig. 4) can be explained by incomplete charge build-up during the shorter light pulses, so that the subsequent hole population decay is not taking place in the very low-field region described.

The model was also able to simulate transients measured with short dark time, a condition which additionally applies to the high-frequency end of the FRS spectra. In such cases, insufficient time is available for discharge, so that the stored ρ^+ profile becomes approximately static for the whole spectral measurement. For this case, the free hole population build-up during the optical pulse and decay (on removing the photoexcitation) can be described by Eq. (5),

$$\Delta p(t) = C\left[1 - e^{\frac{-t}{\tau}}\right](\text{for rise}); \quad \Delta p(t) = C\left[e^{\frac{-t}{\tau}}\right](\text{for decay})$$
(5)

where $C \cong G\tau$, G is the photogeneration rate and τ is some effective hole lifetime. During photocurrent decay, only a fraction of the total injected hole population in the low-field region is extracted to form a current because the IVAP recombination channel removes holes with a time constant τ. The photocurrent decay is due to the decay in the "supply" of holes. This explains both the insensitivity of the measured FRS rate to applied voltage (Fig. 2) and the reduced magnitude of the current transient amplitude for short dark times (and high frequencies) in Fig. 3.

The initial recombination channel IVAP concentration was set at $N_{\text{ivap}} = 7.7 \times 10^{12}$ cm^{-3} (although as previously noted, this refers to the subset of IVAPs which act as efficient recombination centres, and is not meant to be an estimate of the total IVAP population). The concentration of N_{ivap} decreases by one each time a hole is captured, while the concentration of positively charged IVAPs, N_{vap}^+, is incremented up by one.

The modelled high-frequency (extraction current) decay rate as a function of temperature is compared with experimental data in Fig. 5. As the temperature is initially reduced from ambient, the calculated rate can be seen to increase, in agreement with the measured rate, approximately, as $\sim T^{-1.5}$. This power low-temperature dependence predicted by the model reflects the temperature dependence of the capture coefficient used to describe the rate-limiting capture process (charge neutral capture of the hole) in the IVAP-linked carrier recombination scheme. It is consistent with the idea that close to room temperature, carrier build up during light

excitation and the subsequent decay control the transient response. At lower temperatures, defect control of recombination is not expected to dominate current decay; instead, the onset of strong hole trapping at shallow traps (due to slow release) during transport through the bulk of the film dictates the decay rate. The activation energy, 0.2 eV, is the characteristic depth of the hole traps used in the model.
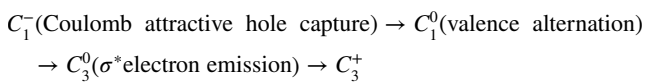
7 Valence alternation defects: energy and charge transfer during photoexcitation

The interpretation and modelling of our experimental data rest on the notion that, under laser excitation, generation of VAPs occurs and the VAP population becomes charge unbalanced ($[C_3^+] \neq [C_1^-]$) due to hole capture. The build-up and decay (following the removal of laser excitation) of the associated charge strongly influences band bending and in turn current flow. Valence alternation defects exhibit a wider spectrum of dynamic properties than is typically used to account for the behaviour of point defects in solids, owing to lone pair-mediated bonding configurations and the charge transfer associated with valence alternation. Here, we add further comments which may reinforce the idea that valence alternation defect kinetics drives the observed optical response. Three principal processes are considered: (1) the high efficiency of hole trapping by isolated VAPs during light excitation, (2) the mechanisms by which IVAPs may promote efficient recombination and (3) the processes involved during a (long) dark period, in which the stored charge relaxes back towards neutrality. Consistent with our low temperature, optically excited EPR measurements, no stable spin active defect states are invoked in our modelling.

7.1 Efficient hole trapping

Positive charging during optical excitation, achieved by the transformation, C_1^- to C_3^+, requires three steps: (i) a change of charge from C_1^- to C_1^0, (ii) a configurational change from C_1^0 to C_3^0 and finally (iii) a further change of charge from C_3^0 to C_3^+. Molecular orbital discussions indicate this complete sequence is exothermic [24]. The initial charging step, $C_1^- \rightarrow C_1^0$, is most likely to involve hole capture given that the C_1^- centres are Coulomb attractive and the supply of holes is large under photoexcitation. This initial step then should be efficient; however, for charge conversion to continue, the hole must remain at the defect and not be returned to the valence band. The neutral dangling bond C_1^0 produced by step (i) is energetically unfavourable in a-Se and is unstable. A lone pair electron is used in a fast bonding configurational change-transforming C_1^0 into to the neutral C_3^0, step (ii). The VAP charge conversion still requires one more positive

charge to be transferred to the defect site. Capture of a second hole at the C_3^0 is of course possible, but likely to be less efficient than step (i) because it is charge neutral. Moreover, the C_3^0 defect is itself unstable and the electron orbital occupancy of C_3^0 may provide a more efficient process: it has one electron occupying an anti-bonding, $\sigma*$ orbital, i.e. close to the bottom of the conduction band and so very weakly bound. The thermal emission rate for the anti-bonding electron, $\omega \sim \omega_0 e^{-\Delta E/kT}$, in the limit that $\Delta E \rightarrow 0$, ω tends to ω_0 which we can assume to be on the order of a phonon frequency. We note that electron emission will also be enhanced by the strong electric fields present in our samples. We suggest, therefore, that for the non-equilibrium conditions established in our experiments, hole capture followed by electron emission, rather than the capture of two holes, is the most likely positive charge storage sequence, although the end result is the same. This results in the overall conversion of C_1^- to C_3^+, i.e.

C_1^-(Coulomb attractive hole capture) $\rightarrow$ C_1^0(valence alternation)

$\rightarrow C_3^0(\sigma^*$electron emission$) \rightarrow C_3^+$

and is described by the single rate coefficient, A_{ivap}^- in Eq. (3). Efficient hole trapping is a well-acknowledged property of a-Se [55, 56]. The VAP route qualitatively described here offers a mechanism for this based on the intrinsic defect population of the material. Note that, in principle, the model does not discriminate between As-based and Se-based valence alternation pair defects as long as the structure has these VAP and IVAP centres. The individual VAPs and IVAPs can involve single or multiple Se chains and can also occur in groups mentioned in Ref. [28].

7.2 Recombination at IVAPs

An IVAP recombination channel has been used to account for transient response in the high-frequency domain, in which equal, exponential rise and decay times are measured. Such exponential carrier build-up and decay would emerge if a single defect type of fixed concentration controlled recombination, such a recombination centre cannot store charge during the recombination process, at least on a time scale that can influence transient response. The suggestion that IVAPs may be efficient recombination centres has been made by several authors (e.g. [47].). Here, we argue that it is the atomic proximity of the positive and negative charges in the IVAP system that may allow this class of defect to act as a significant recombination channel.

In Sect. 6.3, it was noted that the initial hole capture event at C_1^- generates the C_3^0 placing the IVAP momentarily configured as $C_3^0 - C_3^+$. This is a critical point in the overall recombination process because, at least for an *isolated* VAP, the instability of the anti-bonding electron in

the C_3^0 configuration leads to ionisation and generation of C_3^+. We suggest that this does not occur in the case of an IVAP because the weakly bound anti-bonding $\sigma*$ electron at C_3^0 may be spatially stabilised by the close proximity of the positive C_3^+ charge. Provided the dwell time of the σ^* electron is sufficiently long, the positively charged $C_3^0 - C_3^+$ system is now favourable for electron capture. The resulting $C_3^0 - C_3^0$ configuration is of course unstable, but transfer of a single σ^* electron between the two C_3^0 sites will promote configurational change. The latter process is by tunnelling and for IVAPs with small site separation, it occurs on a time scale likely to be short compared with any other in the entire sequence. Bonding reconfiguration finally returns the IVAP to its original and time-averaged $C_3^+ - C_1^-$ form. The recombination event is now complete. There is some similarity between these events and DAP (donor–acceptor pair) recombination: both involve sequential hole and electron capture at an initially charged dipole defect followed by an internal transfer of one electron between the two dipole sites.

7.3 Charge recovery in the dark period

The charge relaxation in the dark has been modelled based on $C_3^+ \rightarrow C_1^-$, as the unbalanced charge in the VAP defect pool returns towards the equilibrium, net charge neutral value. The rate for the process is too slow to influence high-frequency data, but for low frequencies, it has a dominant effect. It occurs on a time scale which is much longer than the time taken for the current to decay as can be seen in Fig. 3.

The charge exchange sequence, $C_3^+ \rightarrow C_1^-$, in the dark is overall endothermic, requiring energy $2E_b + U_{\text{LP}}$, where E_b is the bond energy and U_{LP} is the lone pair electron correlation energy [24]. This energy requirement is qualitatively consistent with a slow process. The sequence can be achieved in principle by either electron capture or hole emission. The relative rates for these processes are not known, but the overall time constant from the experiments can be estimated to be approximately 65 ms. In this model, we have described the dark relaxation process as sequential capture of two electrons from the electron component of the dark current flowing in the structure. An alternative explanation is based on the emission of two holes as observed in a-As$_2$Se$_3$ films [57]. However, the data reported in [57] were taken under very different non-equilibrium conditions to ours viz. open circuit conditions (xerographic dark discharge).

We modelled the first event in the process as electron capture into the Coulomb attractive C_3^+, generating C_3^0 with no bonding reconfiguration. Efficient loss of this anti-bonding electron at this stage facilitates the back transformation; indeed, one might envisage that the process $C_3^0 \rightarrow C_3^+ + e^-$ might be stochastically selected many times before a dwell

time of the electron is sufficiently long to accommodate the capture of a second electron. This would explain the slow rate of discharge. Upon the capture of the second electron, C_3^0 rapidly undergoes an exothermic bonding configuration change to produce the stable C_1^- defect. The endothermic charge relaxation can be viewed as the thermodynamic drive to recover overall neutrality, with volume Coulomb charging energy and strain energy minimised on a long time scale.

8 Conclusions

We have investigated the transient photocurrent behaviour of a-Se using both FRS and single transient analysis with variable dark period recovery times. For both measurements, complicated "non-ideal" behaviour is observed. For example, the FRS quadrature signal exhibits a distinct peak in the kilohertz range, the position of which is independent of the light intensity and applied voltage, but has some sample-to-sample dependence. The low-frequency in-phase and quadrature photocurrents evince anomalous behaviour with the quadrature signal becoming negative with a very broad shoulder or peak. By measuring photocurrent transients, however, we are able to show that the form of the transient depends critically on the relative time spent by the material in the light during pulse excitation and time spent in the dark undergoing recovery. This is the origin of the distortion of FRS spectra observed at low frequencies.

A model to simulate and understand photocurrent transients has been described using numerical and simultaneous solution of Poisson's equation, and the electron and hole continuity equations with charge exchange rate equations. The model specifically includes the field and temperature dependence of the photogeneration process in a-Se in the photogeneration region. The model established that the distortion of the electric field profile due to strong near-surface charging plays a key role in determining the transient response. Positive charging (hole trapping) in the near-surface region of the structure that encompasses the photogeneration region was found to be essential in order to explain the symmetrical, near-exponential transients at high frequencies (with short dark pulse) and the large transient overshoots which occur after long dark pulses. A specific attribute of the model is the use of valence alternation pair (VAP) defects in trapping and recombination processes and also the interconversion between these VAP defects to account for the kinetics of charge transfer. The light-induced creation of long-lived spin active defects were excluded in the model based on the lack of the EPR signal in samples illuminated with a 405 nm laser beam at 10 W cm^{-2} down to 5 K.

We have demonstrated that valence alternation pair (VAP) defects provide a plausible route for charge storage and we further suggest that the properties of IVAPs account for the main recombination channel. A particular property of VAP defects in a-Se is that they are readily generated and converted by light excitation, which provides an efficient route to preferential near-surface charge storage. By using this process within our simulations, good agreement for the rather complex variation in transient shapes was obtained. VAPs are responsible for many properties of a-Se; here, we have demonstrated that the role played by VAPs in trapping and recombination can be sensed using photocurrent spectroscopy in the frequency domain with photocurrent transients in the time domain. The ability of the light-induced VAP model (and associated charge exchange processes) to reproduce the transient photocurrent response demonstrates that VAP defects may play an important role in the dynamic optical response of a-Se. This finding supports similar conclusions for X-ray response [40] concerning the reduction in sensitivity of a-Se X-ray detectors upon exposure to high-dose radiation.

References

1. K. Ahluwalia, *Applications of Chalcogenides: S, Se, and Te* (Springer, New York, 2016). https://doi.org/10.1007/978-3-319-41190-3

2. K. Tanaka and K. Shimakawa, *Amorphous Chalcogenide Semiconductors and Related Materials* (Springer, New York, 2011). https://doi.org/10.1007/978-1-4419-9510-0 (See also references therein.)

3. V.I. Mikla, V.V. Mikla, *Amorphous Chalcogenides: The Past, Present and Future* (Elsevier, Amsterdam, 2012)

4. V.I. Mikla, V.V. Mikla, *Medical Imaging Technology* (Elsevier, Amsterdam, 2014)

5. A. V. Kolobov, J. Tominaga, P. Fons, Phase-change memory materials, in *Springer Handbook of Electronic and Photonic Materials*, 2nd edn (Springer, New York, 2017). https://doi.org/10.1007/978-3-319-48933-9_46

6. J.C. Schottmiller, J. Vac. Sci. Technol. **12**, 807 (1975). https://doi.org/10.1116/1.568676

7. S.O. Kasap, K.V. Koughia, B. Fogal, G. Belev, R.E. Johanson, Semiconductors **37**, 789 (2003)

8. G.S. Belev, B. Fogal, K.V. Koughia, R.E. Johanson, S.O. Kasap, J. Mater. Sci. Mater. Electron. **14**, 841 (2003). https://doi.org/10.1023/A:1026150514758

9. S. Kasap et al., Sensors **11**, 5112–5157 (2011). https://doi.org/10.3390/s110505112

10. M. Mitkova, D.P. Butt, Chalcogenide glass ionizing radiation sensor, US Patent No. US8466425B2 (2011)

11. M.S. Ailavajhala, Y. Gonzalez-Velo, C.D. Poweleit, H.J. Barnaby, M.N. Kozicki, D.P. Butt, M. Mitkova, J. Hazard. Mater. **269**, 68–73 (2014). https://doi.org/10.1016/j.jhazmat.2013.11.050

12. M.S. Ailavajhala, Y. Gonzalez-Velo, C. Poweleit, H. Barnaby, M.N. Kozicki, K. Holbert, D.P. Butt, M. Mitkova, J. Appl. Phys. **115**, 043502 (2014). https://doi.org/10.1063/1.4862561

13. S. Imura, K. Mineo, K. Miyakawa, M. Nanba, H. Ohtake, M. Kubota, Sensors J. IEEE **18**, 3108–3113 (2018). https://doi.org/10.1109/JSEN.2018.2809477

14. J. D. John, N. Miyachi, K. Enomoto, M. Tsuzaki, R. Mori, R. Umezawa, T. Takahashi, I. Saito, K. Okano, T. Masuzawa, T. Yamada, International Vacuum Nanoelectronics Conference (IVNC), Kyoto, Japan, 9–13 (2018). https://doi.org/10.1109/IVNC.2018.8520023

15. J.D. John, I. Saito, R. Toyama, J. Ochiai, T. Yamada, T. Masuzawa, D.H.C. Chua, K. Okano, Electron. Lett. **53**, 1270–1272 (2017). https://doi.org/10.1049/el.2017.1413

16. J.R. Scheuermann, A.H. Goldan, O. Tousignant, S. Léveillé, W. Zhao, Med. Phys. **42**(3), 1223–1226 (2015). https://doi.org/10.1118/1.4907971

17. J.R. Scheuermann, Y. Miranda, H. Liu, W. Zhao, J. Appl. Phys. **119**, 024508 (2016). https://doi.org/10.1063/1.4939602

18. M. Zhu, G. Niu, J. Tang, J. Mater. Chem. C **7**, 2199–2206 (2019). https://doi.org/10.1039/C8TC05873C

19. S. Imura, T. Watabe, K. Miyakawa, K. Hagiwara, H. Ohtake, M. Kubota, J. Mater. Sci. Mater. Electron **28**, 7064–7069 (2017). https://doi.org/10.1007/s10854-016-6311-6

20. K. Tanaka, Amorphous selenium and nanostructures, in *Springer Handbook of Glass*. (Springer, Cham, 2019). https://doi.org/10.1007/978-3-319-93728-1_19

21. O. Güneş, C. Koughia, R.J. Curry, A.B. Gholizadeh, G. Belev, K.O. Ramaswami, S.O. Kasap, J. Mater. Sci. Mater. Electron. **30**, 1 (2019). https://doi.org/10.1007/s10854-019-01386

22. J.B. Frey, K. Sadasivam, G. Belev, H. Mani, L. Laperriere, S. Kasap, J. Vac. Sci. Technol. A **37**, 061501 (2019). https://doi.org/10.1116/1.512119

23. D. Adler, E.J. Yoffa, Can. J. Chem. **95**, 1920 (1977)

24. M. Kastner, D. Adler, H. Fritzsche, Phys. Rev. Lett. **37**, 1504–1507 (1976). https://doi.org/10.1103/PhysRevLett.37.1504

25. R.A. Street, N.F. Mott, Phys. Rev. Lett. **35**, 1293–1296 (1975). https://doi.org/10.1103/PhysRevLett.35.1293

26. P.W. Anderson, Phys. Rev. Lett. **34**, 953 (1975). https://doi.org/10.1103/PhysRevLett.34.953

27. D. Drabold, X. Zhang, J. Li, First principles molecular dynamics and photo structural response in amorphous silicon and chalcogenide glasses, in *Photo-Induced Metastability in Amorphous Semiconductors* (Wiley-VCH, Weinheim, 2003). https://doi.org/10.1002/9783527602544.ch15

28. J. Berashevich, A. Mishchenko, A. Reznik, Phys. Rev. Appl. **1**, 034008 (2014). https://doi.org/10.1103/PhysRevApplied.1.034008

29. A.V. Kolobov, M. Kondo, H. Oyanagi, A. Matsuda, K. Tanaka, Phys. Rev. B **58**, 12004–12010 (1998). https://doi.org/10.1103/PhysRevB.58.2004

30. X. Zhang, D.A. Drabold, Int. J. Mod. Phys. B **15**, 3190–3196 (2001). https://doi.org/10.1142/S0217979201007476

31. S.A. Dembovsky, E.A. Chechetkina, Hypervalent bonds as active centers providing photo-induced transformations in glasses, in *Photo-Induced Metastability in Amorphous Semiconductors* (Wiley-VCH, Weinheim, 2003), pp. 299–309. https://doi.org/10.1002/9783527602544.ch17

32. D. Carles, G. Lefrancoise, J.P. Larmagnac, J. Phys. Lett. **45**, L901–L906 (1984)

33. M.L. Benkhedir, M.S. Aida, G.J. Adriaenssens, J. Non-Cryst. Solids **344**, 193 (2004). https://doi.org/10.1016/j.jnoncrysol.2004.08.062

34. M.L. Benkhedir, M.S. Aida, N. Qamhieh, A. Stesmans, G.J. Adriaenssens, J. Optoelectron. Adv. Mater. **7**, 329 (2005)

35. K. Shimakawa, K. Fukami, H. Kishi, G. Belev, S. Kasap, Jpn. J. Appl. Phys. **46**, L192 (2007). https://doi.org/10.1143/JJAP.46.L192

36. M.L. Benkhedir, M. Mansour, F. Djefaflia, M. Brinza, G.J. Adriaenssens, Phys. Status Solidi B **246**, 1841–1844 (2009). https://doi.org/10.1002/pssb.200982014

37. A.V. Kolobov, J. Tominga, Reversible photostructural changes, in *Chalcogenides Metastability and Phase Change Phenomena* (Springer, New York, 2012) (See also references therein). https://doi.org/10.1007/978-3-642-28705-3_4

38. S. Kasap, C. Koughia, J. Berashevich, R. Johanson, A. Reznik, J. Mater. Sci. Mater. Electron. **26**, 4644 (2015). https://doi.org/10.1007/s10854-015-3069-1

39. C. Koughia, A. Reznik, C. Allen, R. Johanson, S. Kasap, Phys. Status Solidi A **213**, 1856–1863 (2016)

40. F. Manouchehri, M.Z. Kabir, O. Tousignant, H. Mani, V.K. Devabhaktuni, J. Phys. D Appl. Phys. **41**, 235106 (2008)

41. G. Belev, S. Kasap, J. Non-Cryst, Solids **345**, 484–488 (2004). https://doi.org/10.1016/j.jnoncrysol.2004.08.070

42. B. Fogal, S. Kasap, Can. J. Phys. **92**, 634–640 (2014). https://doi.org/10.1139/cjp-2013-0524

43. S.O. Kasap, J. Yang, B. Simonson, E. Adeagbo, M. Walornyj, G. Belev, M.P. Bradley, R.E. Johanson, J. Appl. Phys. **127**, 084502 (2020). https://doi.org/10.1063/1.5140599

44. D.M. Hunter, J.A. Rowlands, J. Mater. Sci. Mater. Electron. (2020). https://doi.org/10.1007/s10854-020-03441-4

45. M. Tabak, M. Scharfe, J. Appl. Phys. **41**, 2114 (1970). https://doi.org/10.1063/1.1659174

46. G. Belev, S. Kasap, J. Optoelec, Adv. Mater. **9**, 1–10 (2007)

47. R.A. Street, Solid State Commun. **24**, 363 (1977)

48. S. Kasap, J.B. Frey, G. Belev, O. Tousignant, H. Mani, L. Laperriere, A. Reznik, J.A. Rowlands, Phys. Status. Solidi B **246**, 1794–1805 (2009). https://doi.org/10.1002/pssb.200982007

49. K. Shimakawa, A. Kolobov, S.R. Elliott, Adv. Phys. **44**, 475–588 (1995)

50. M.D. Tabak, P.J. Warter, Phys. Rev. **173**, 899 (1968). https://doi.org/10.1103/PhysRev.173.899

51. W. Shockley, W.T.J. Read, Phys. Rev. **87**(5), 835–842 (1952). https://doi.org/10.1103/PhysRev.87.835

52. P. Langevin, Ann. Chim. Phys. **28**, 433 (1903)

53. K. Koughia, Z. Shakoor, S.O. Kasap, J.M. Marshall, J. Appl. Phys. **97**, 033706 (2005). https://doi.org/10.1063/1.1835560

54. M. Lax, Phys. Rev. **119**, 1502 (1960). https://doi.org/10.1103/PhysRev.119.1502

55. K. Koughia, S. Kasap, J. Non-Cryst, Solids **352**, 1539 (2006). https://doi.org/10.1016/j.jnoncrysol.2005.10.031

56. S.M. Arnab, M.Z. Kabir, J. Appl. Phys. **122**, 134502 (2017). https://doi.org/10.1063/1.5000510

57. A.R. Melnyk, J. Non-Cryst, Solids **35**, 837 (1980). https://doi.org/10.1016/0022-3093(80)90304-X